Supplementary Information for

Carbon-based Catalysts by Structural Manipulation with Iron for Oxygen Reduction Reaction

Yao Wang,[†] Wei Chen,[†] Yong Chen,[‡] Bin Wei,[‡] Linhui Chen,[†] Lishan Peng,[†] Rui Xiang,[†]
Jing Li,[†] Zhongchang Wang,[*,‡] and Zidong Wei[*,†]

[†]Chongqing Key Laboratory of Chemical Process for Clean Energy and Resource Utilization, College of Chemistry and Chemical Engineering, Chongqing University, Chongqing 400044, China

[‡]Department of Quantum Materials Science and Technology, International Iberian Nanotechnology Laboratory (INL), Av. Mestre José Veiga s/n, Braga 4715-330, Portugal

Figure S1

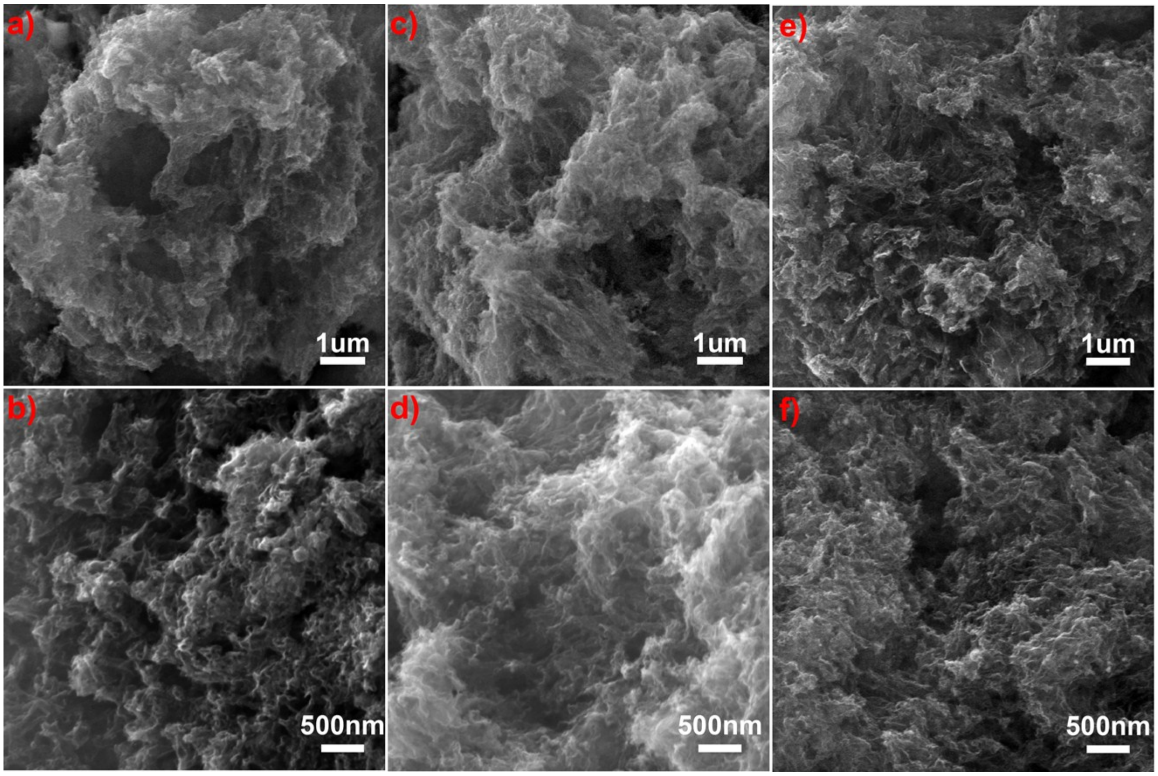

Figure S1. SEM images of the as-prepared catalysts: (a,b) Fe-N-G-120, (c,d) Fe-N-G-180, and (e,f) Fe-N-G-360.

Figure S2

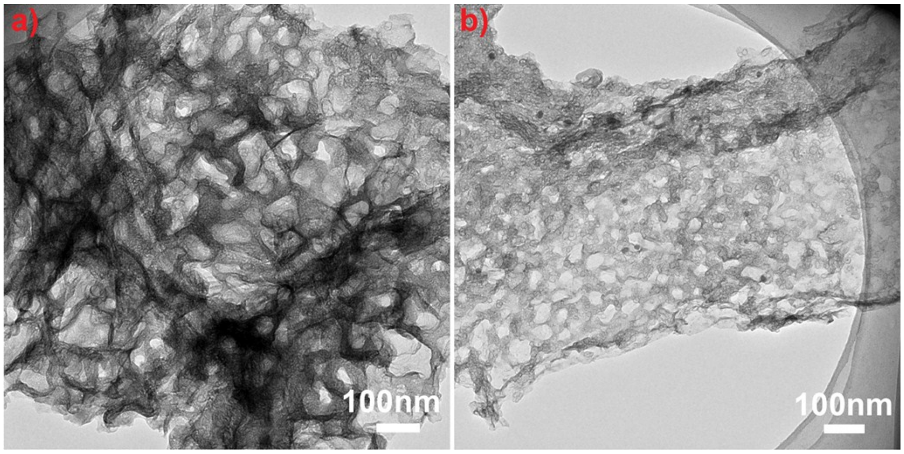

Figure S2. TEM images of the as-prepared Fe-N-G-240 catalyst taken in different areas.

Figure S3

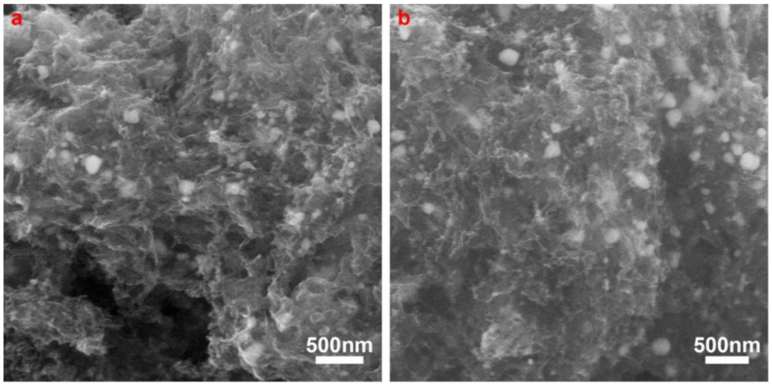

Figure S3 The SEM images of as-prepared Fe-N-G-240 catalyst without acid treatment

Figure S4

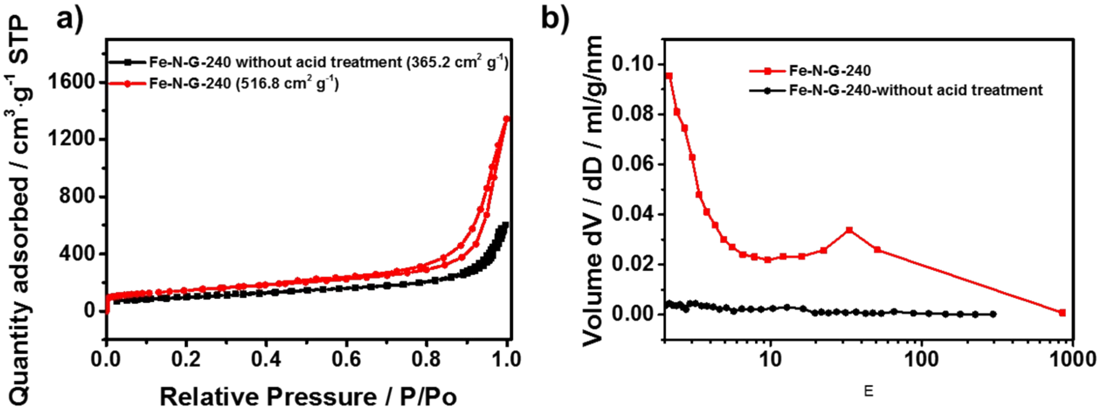

Figure S4 (a) N_2 adsorption-desorption isotherms and (b) distribution of mesopore size of the Fe-N-C-240 catalyst with or without acid treatment. The increase in the BET surface area and mesopore volume confirms that the aggregated metal nanoparticles are etched, leaving the pores for easy mass transport.

Figure S5

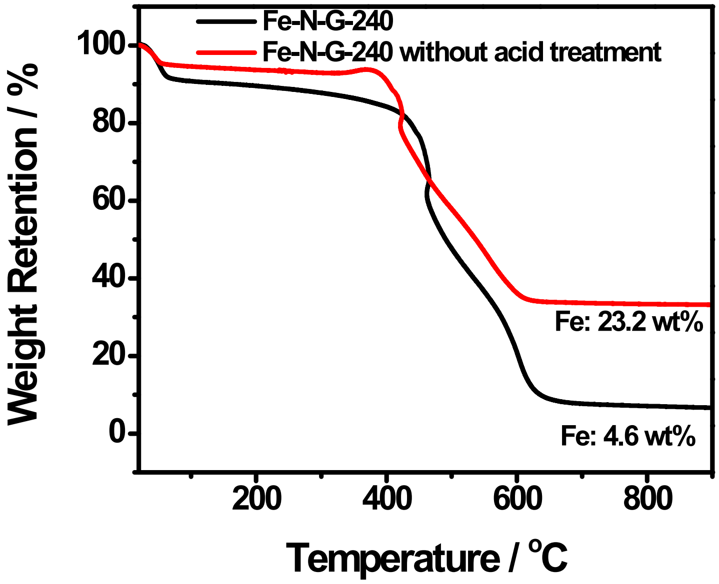

Figure S5 The TGA curves of the Fe-N-G-240 catalysts with or without acid treatment. The decrease of the Fe content demonstrates that most of Fe nanoparticles are removed by acid treatment.

Figure S6

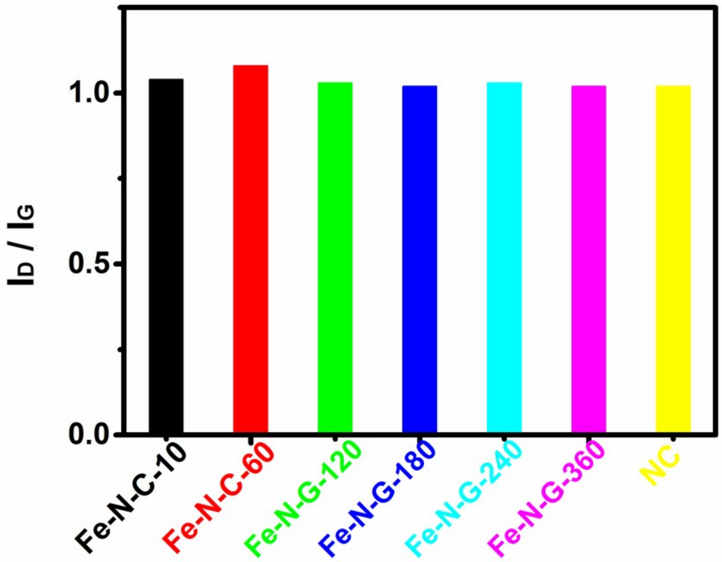

Figure S6. Intensity ratio of the D to G band (I_D/I_G) for the catalysts.

Figure S7

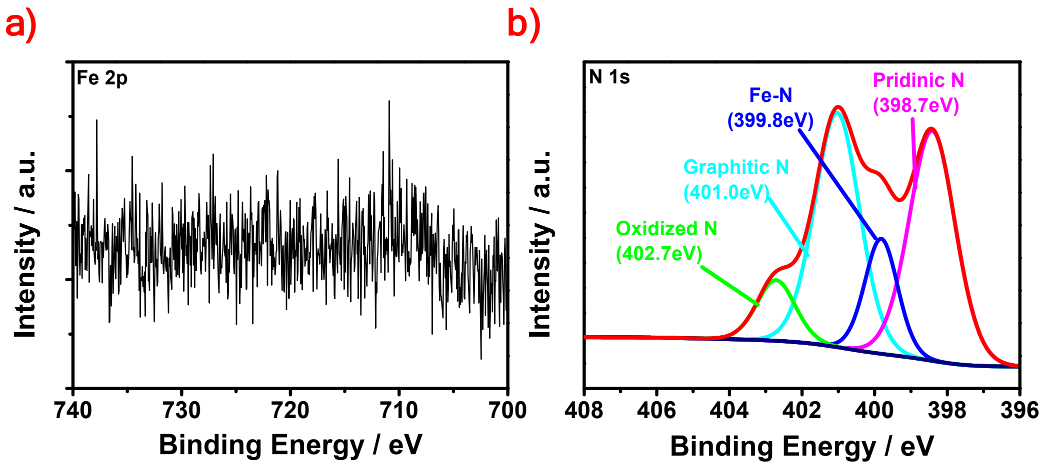

Figure S7. High-resolution Fe 2p and N 1s XPS spectra for the Fe-N-G-240 sample.

Figure S8

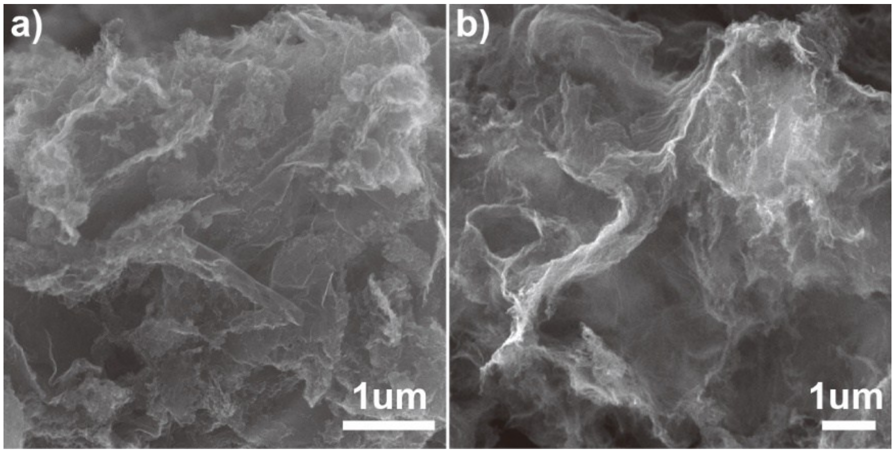

Figure S8. SEM image of the catalysts fabricated by replacing the urea with (a) melamine and (b) thiourea as the nitrogen precursor.

Figure S9

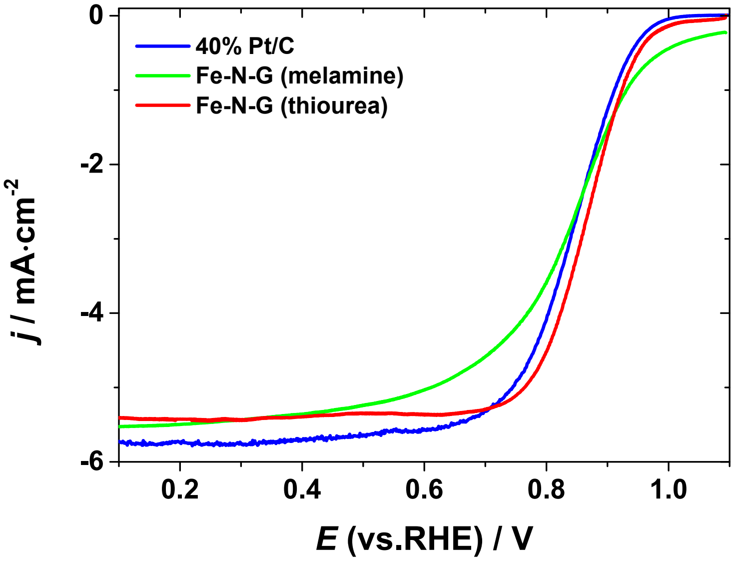

Figure S9. The LSV curves for the catalysts prepared using melamine and thiourea as the nitrogen precursor in O_2 saturated KOH.

Figure S10

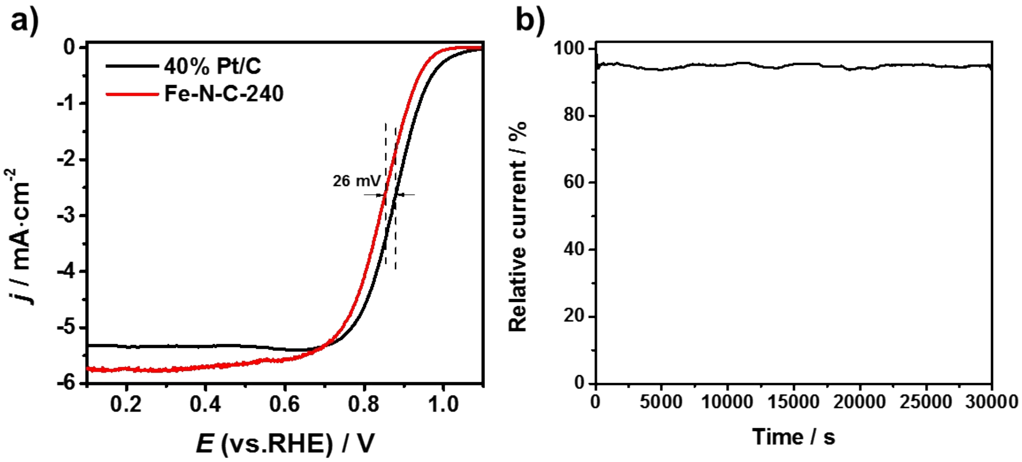

Figure S10. (a) Linear sweep voltammograms (LSV) curves of the Fe-N-G catalyst (0.6 mgcm^{-2}) and the Pt/C (25 ug Pt cm^{-2}) at a rotation rate of 1600 rpm in an O_2-saturated 0.1 M KOH. The scan rate is 10 mVs^{-1}. (b) ADT test of Fe-N-G-240 in O_2-saturated 0.1 M KOH at a rotation rate of 900 rpm under 0.7V (vs. RHE).

Figure S11

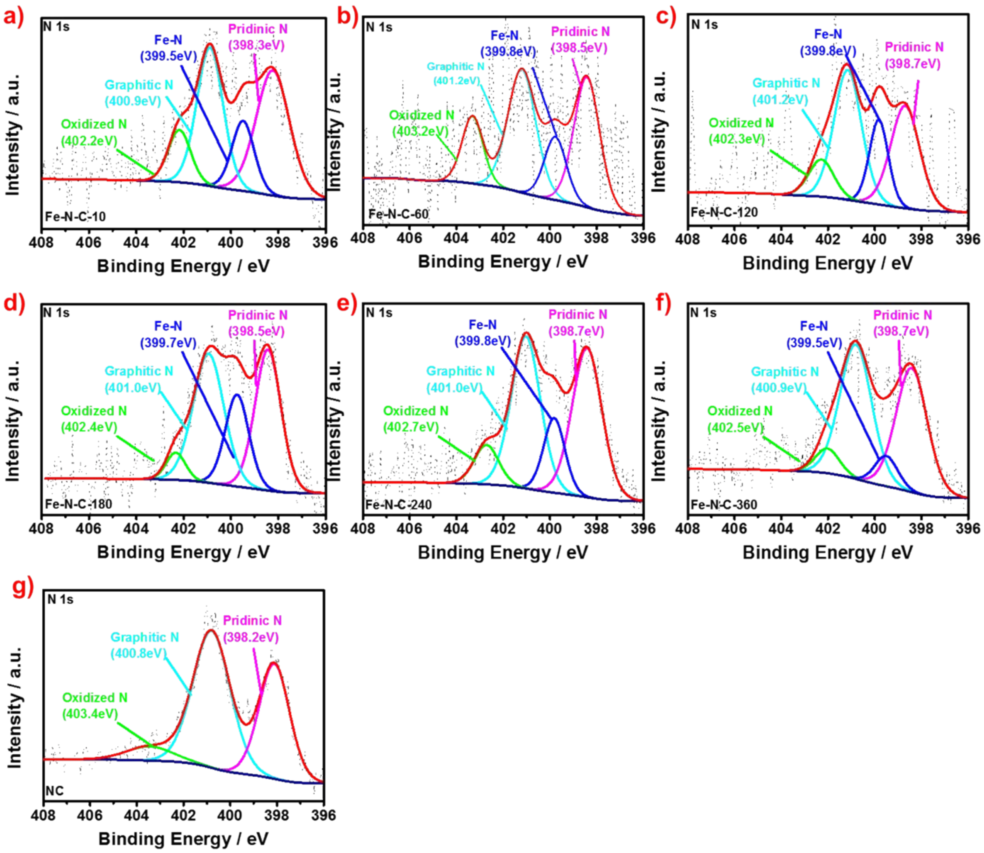

Figure S11 XPS spectra of N 1s for the all catalysts: (a) Fe-N-C-10, (b) Fe-N-C-60, (c) Fe-N-G-120, (d) Fe-N-G-180, (e) Fe-N-G-240, (f) Fe-N-G-360, and (g) NC.

Figure S13

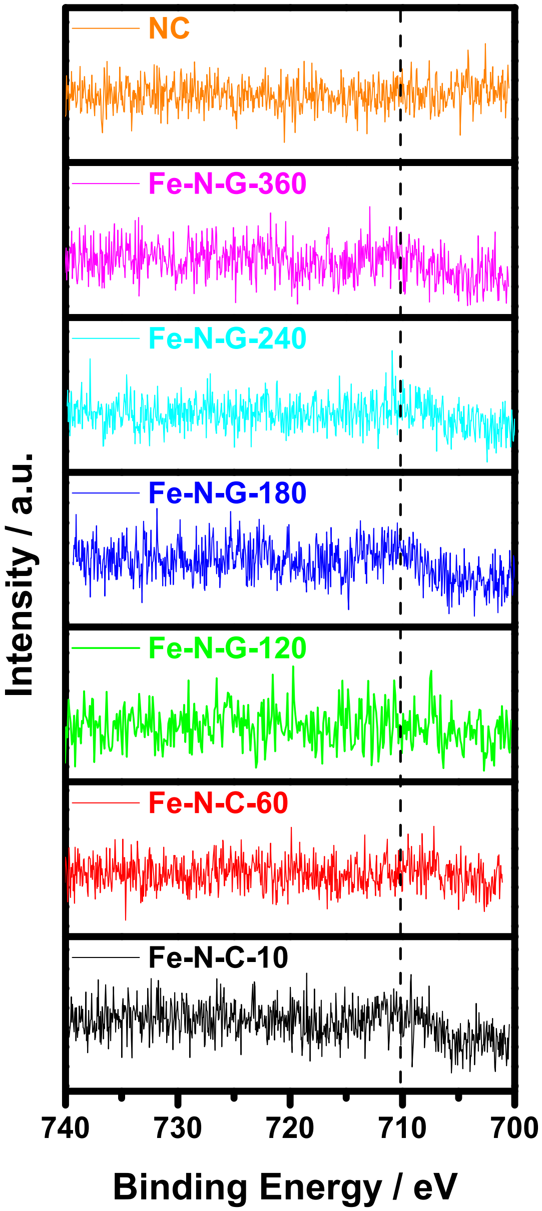

Figure S12 XPS spectra of Fe 2p for all the catalysts.

Figure S13

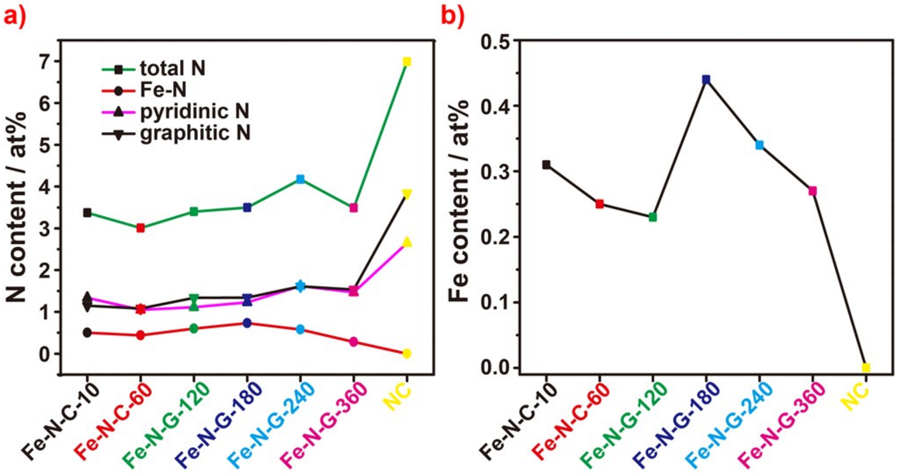

Figure S13. (a) Nitrogen and (b) Fe content calculated from the XPS spectrum for all the catalysts.

XPS analysis was employed to better understand the detailed surface elemental composition and state of all the catalysts. As shown in Fig. S11, the XPS spectra of N 1s for all the catalysts have been carefully deconvoluted into four nitrogen species, including pyridinic N, Fe-N, graphitic N and oxidized N. The nitrogen content in Fe-N-C catalysts is 3.37 at% for Fe-N-C-10, 3.01 at% for Fe-N-C-60, 3.40 at% for Fe-N-G-120, 3.50 at% for Fe-N-G-180, 4.17 at% for Fe-N-G-240, 3.49 at% for Fe-N-G-360, 6.99 at% for NC, respectively. After deconvolution, the content of pyridinic N, Fe-N and graphitic N were calculated and their corresponding results are shown in Fig. S13. It is can be seen that the NC has the highest pyridinic N (2.65 at%) content as well as the highest graphitic N (3.84 at%) content. Apart from the NC catalysts, the Fe-N-G-240 catalyst possesses the highest pyridinic N and graphitic N content, and the Fe-N-G-180 catalyst possesses the highest Fe-N content. It is also noteworthy that there exists Fe on the surface of Fe-N-G catalysts. As shown in Fig. S12, the signal is only appeared around 710 eV, which is considered as Fe in Fe−N$_x$ configuration. The content of Fe in the catalysts is also summarized in Fig.

S8b. Obviously, the Fe-N-C has the highest Fe content, which is consistent with the result gained from the N 1s spectra. Thus, Fe is effectively doped into carbon matrix to produce Fe-N_x. However, there is no distinctive linear relationship between the Fe (N) content in the final catalysts and the content of $FeCl_3$ in precursors, which means that the doped Fe or N is associated with other factors. Taking the morphology into consideration, since the Fe-N-C-10 and Fe-N-C-60 contain CNT, it can be concluded that much amount of $FeCl_3$ in the precursors can accelerate the doping process by the formation of a highly graphited structure. On the contrary, the Fe-N-C catalysts with a similar morphology of crumpled nanoporous graphene show different phenomenon. With the decrease of the addition of $FeCl_3$ in the precursors, the content of N increases firstly to the maximum and then decreases, demonstrating that an appropriate amount of $FeCl_3$ has a positive effect on the N doping. As for the content of Fe on the surface of the catalysts, a similar phenomenon can be observed, suggesting that there is no positive correlation between the addition of $FeCl_3$ and the content of doped Fe. Based on the aforementioned formation mechanism of catalysts, this phenomenon may be caused by a dynamic equilibrium between the Fe agglomeration and the Fe doping process.

Figure S14

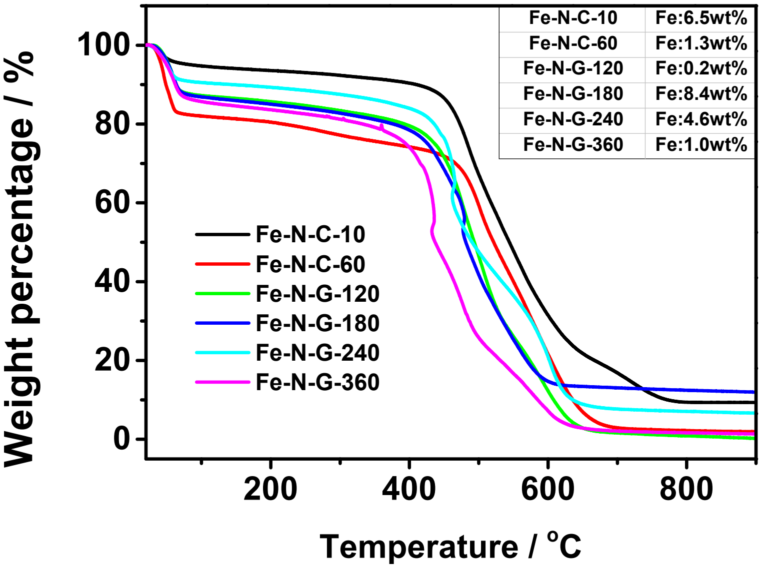

Figure S14 TGA curves of all the catalysts.

Figure S15

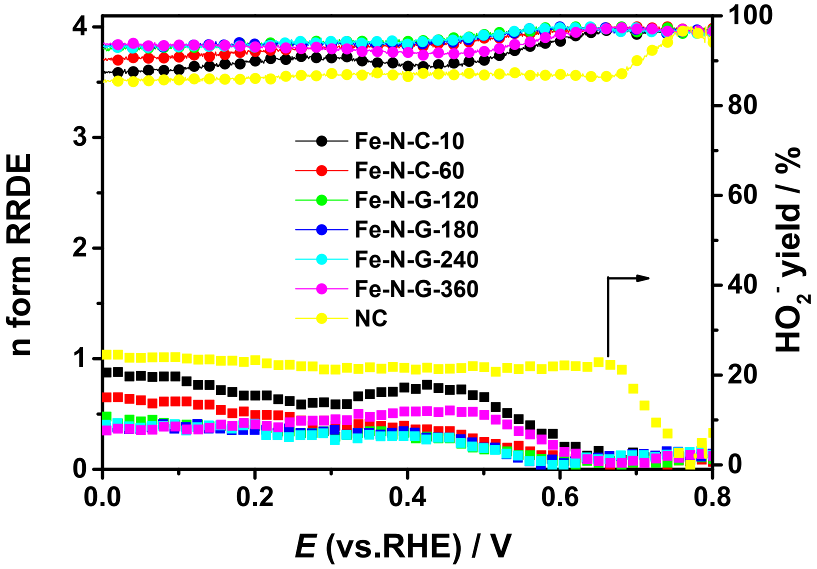

Figure S15. The electron transfer number (n) and the HO_2^- yield derived from the RRDE test.